Anthropogenic fill and geological–hydrological controls on progressive failure in the 2023 Stenungsund quick-clay landslide (SW Sweden)

Christian Öhrling[1,2*] and Ola Fredin[1]
[1*]Department of Geosciences, Norwegian University of Science and Technology (NTNU), Trondheim, Norway.
[2]Department of Quaternary Geology, Geological Survey of Sweden, Gothenburg, Sweden.

*Corresponding author(s). E-mail(s): christian.ohrling@ntnu.no;
Contributing authors: ola.fredin@ntnu.no;

Abstract

On 23 September 2023, a rapid quick-clay landslide occurred at the Stenungsund interchange on the E6 highway in southwestern Sweden, severely damaging national and local infrastructure and closing a key transport corridor for 285 days. The landslide affected approximately 15 ha, with a runout of 620 m and an estimated displaced volume of 1.2–1.85 million m³. This study reconstructs the geological, hydrological, and anthropogenic conditions that led to failure by integrating field observations, stratigraphic and geotechnical data, LiDAR-based elevation models, aerial and satellite imagery, and hydrological flow modeling.

The site is underlain by thick late- and postglacial marine clays interbedded with permeable silt, sand, and shell-rich layers within a fracture-valley landscape. These sediments facilitated groundwater flow and salt leaching, resulting in high clay sensitivity. Results suggest initiation as a deep-seated translational progressive failure beneath anthropogenic fill, as inferred from finite element modeling and field observations/stratigraphy. Construction-related loading was interpreted as the primary trigger, while altered drainage patterns, increased infiltration along fractured bedrock, and elevated pore-water pressures—likely intensified by heavy rainfall shortly before the event—controlled the timing and magnitude of the failure. Loss of resistance downslope enabled the rapid mobilization of quick clay and resulted in large horizontal displacements.

The Stenungsund event demonstrates how cumulative anthropogenic modifications can destabilize sensitive clay slopes. The findings highlight the importance of integrated geological–hydrogeological assessments in infrastructure planning and the need for improved risk management in quick-clay terrain.

Keywords: quick clay, infrastructure, translational-progressive landslide, anthropogenic, geology

Introduction

Quick-clay landslides are among the most serious geohazards in Scandinavia, with a long record of destructive events in Sweden and Norway. These landslides occur in sensitive clays of marine origin that were deposited during the last deglaciation and subsequently uplifted above sea level. When remoulded, these clays lose much of their shear strength, making them prone to rapid progressive failures with long runout distances (Torrance 2012). Historical events in Scandinavia demonstrate severe societal impacts in sensitive clays (e.g. Caldenius et al. 1956; Odenstad 1958; Hartlén 1984; SHK 2009; Ryan et al. 2021). The Munkedal event disrupted the European route E6 highway

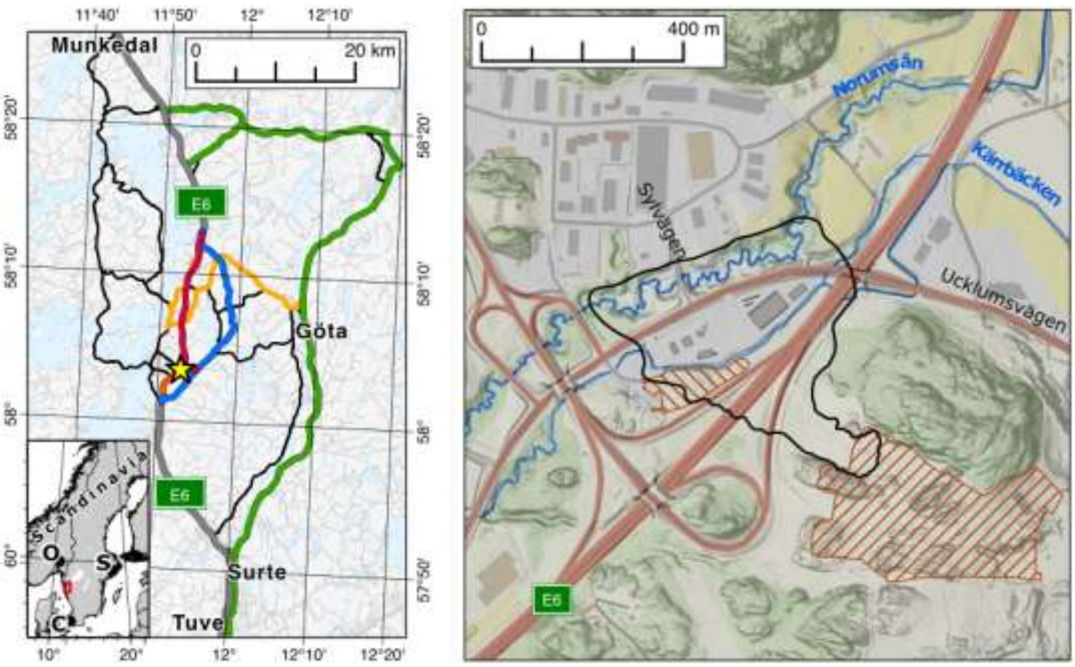

Fig. 1 **a** The Swedish west coast contains widespread marine clays prone to quick-clay formation. The 23 September 2023 landslide occurred at the Stenungsund interchange on the E6 in southwestern Sweden (yellow star). Road closures rerouted traffic: the designated Gothenburg–Oslo diversion is shown in green, while the largest increases occurred on local roads (blue) and other routes with elevated heavy traffic (orange/black), several of which required repaving and reinforcement. Many major landslides have occurred in the region; four examples are: Surte (1950), Göta (1957), Tuve (1977), and Munkedal (2006). **b** The landslide area is outlined by the black polygon; red hatching shows active construction. Norumsån and the spring-fed Kärrbäcken traverse the area. Background: Topographic and elevation data © Lantmäteriet.

(hereafter, 'E6') for several months. During manuscript preparation, another quick-clay landslide occurred on the E6 north of Trondheim on 30 August 2025, resulting in one fatality (Nikel 2025).

At around 01:40 a.m. on 23 September 2023, a large landslide occurred at the Stenungsund interchange on the E6 in southwestern Sweden (58°3'33"N 11°52'55"E) (Fig. 1). The event displaced 15 hectares of soil and construction materials, tore apart both the E6 and a municipal road, dammed a small river, and destroyed several commercial buildings. Within the landslide area, nine cars and one bus were trapped while driving, and eleven professional drivers were in their parked trucks. Fortunately, no fatalities occurred – largely due to the timing of the event at night, when traffic and commercial activity were minimal. Nevertheless, the event caused severe economic disruption, blocking the main transport artery between Oslo and continental Europe, highlighting the vulnerability of infrastructure in sensitive clay terrain.

Road closures impose substantial socioeconomic costs. At Stenungsund, reconstruction costs were approximately US$54 million (national) and approximately US$27 million (municipal), and detour-related transport costs were estimated at approximately US$122–253 million over 285 days (Åberg et al. 2023). Rerouted traffic also increased the risk of accidents: 17 accidents occurred on road 650 during the closure (Fig. 1a), including a fatal frontal collision, compared to an average of 4.5 accidents per corresponding-year interval (two fatal) over the 19 years before and one year after (The Swedish Transport Agency). Although precise quantification is difficult, the Stenungsund case underscores how landslide-related road closures impose significant social, economic, and environmental costs, highlighting the need for proactive risk management and resilient infrastructure.

The Stenungsund landslide offers an important case study of how geological predisposition, hydrological variability, and anthropogenic modification interact to trigger large-scale failures in sensitive clays. The site lies within the fracture-valley landscape in southwestern Sweden. The bedrock consists primarily of deformed gneisses and granitoids of Sveconorwegian age, overlain by Quaternary deposits. Deglaciation processes, land uplift, shoreline displacement, and postglacial marine processes have contributed to the character of thick clay sequences in valley bottoms, creating conditions favorable for quick-clay development.

Heavy rainfall in September 2023, combined with changes in surface water drainage due to construction activities, likely contributed to elevated pore-water pressures in clay and surface erosion. At the time of failure, ongoing infrastructure development was taking place on both sides of the E6, modifying the local topography and imposing additional loads on the ground surface. Post-landslide calculations by the Swedish Geotechnical Institute (SGI) show that the area had satisfactory stability before the development in 2023 (Isacsson et al. 2025).

We examine the Stenungsund landslide by documenting pre- and post-failure conditions and analyzing stratigraphic, hydrological, and anthropogenic controls. Using fieldwork, digital elevation models (DEMs), satellite (optical/InSAR), aerial imagery, and geotechnical data, we assess how these factors governed initiation and progression — with implications for hazard assessment and land-use planning in sensitive-clay terrain.

Study area and geological setting

South-western Sweden is characterized by a distinct fracture-valley landscape formed through the removal of material during the Cenozoic that had accumulated in Precambrian fractures as a product of deep weathering during the Mesozoic (Lidmar-Bergström 1997). Elevated plateaus represent remnants of a sub-Cambrian peneplain that developed during prolonged pre-Quaternary erosion of the upper crust (Lidmar-Bergström 1982). Subsequent differential erosion by fluvial systems produced a dissected landscape of valleys aligned with bedrock structures. These features were further reshaped during the Pleistocene glaciations, when advancing and retreating ice sheets eroded and deepened existing depressions (Fredén 1987).

The bedrock in the Stenungsund area consists of a granitoid intrusion within the Idefjord terrain, dated to 1,522 ± 10 Ma (Åhäll 1990; Åhäll and Connelly 2008). Gneiss and granite show variable deformation (folding, fracturing, and mylonites). Deformation intensity depends on lithology and proximity to tectonic zones, which are linked to the Sveconorwegian orogeny (1,150—900 Ma). Extensive fracture and fault zones strongly influence groundwater flow and slope stability (Fig. 2).

The Quaternary deposits of southwestern Sweden reflect a complex interplay of glacial and postglacial processes. The highest paleo coastline raised by glacial-isostatic rebound is located at approximately 125 m above sea level (a.s.l.), and widespread glaciomarine and postglacial clays occupy valley bottoms (SGU 2024), with thicknesses ranging from 10 to 50 m in the area of the landslide. Ice margin retreat produced moraine ridges and glaciofluvial outwash deposits, while the marine-terminating setting left thick sequences of glaciomarine clay (Fig. 2). The hills in the region stand at 150 m a.s.l., and the sea-reaching valleys rise to around 40 m a.s.l. These deposits provide the basis for quick-clay formation when infiltrating freshwater causes binding salt ions to leach. The porosity and structure of these clays make them vulnerable to collapse under mechanical or hydraulic stress. The landslide area rose above sea level approximately 11,000 years ago (e.g. Stroeven et al. 2016).

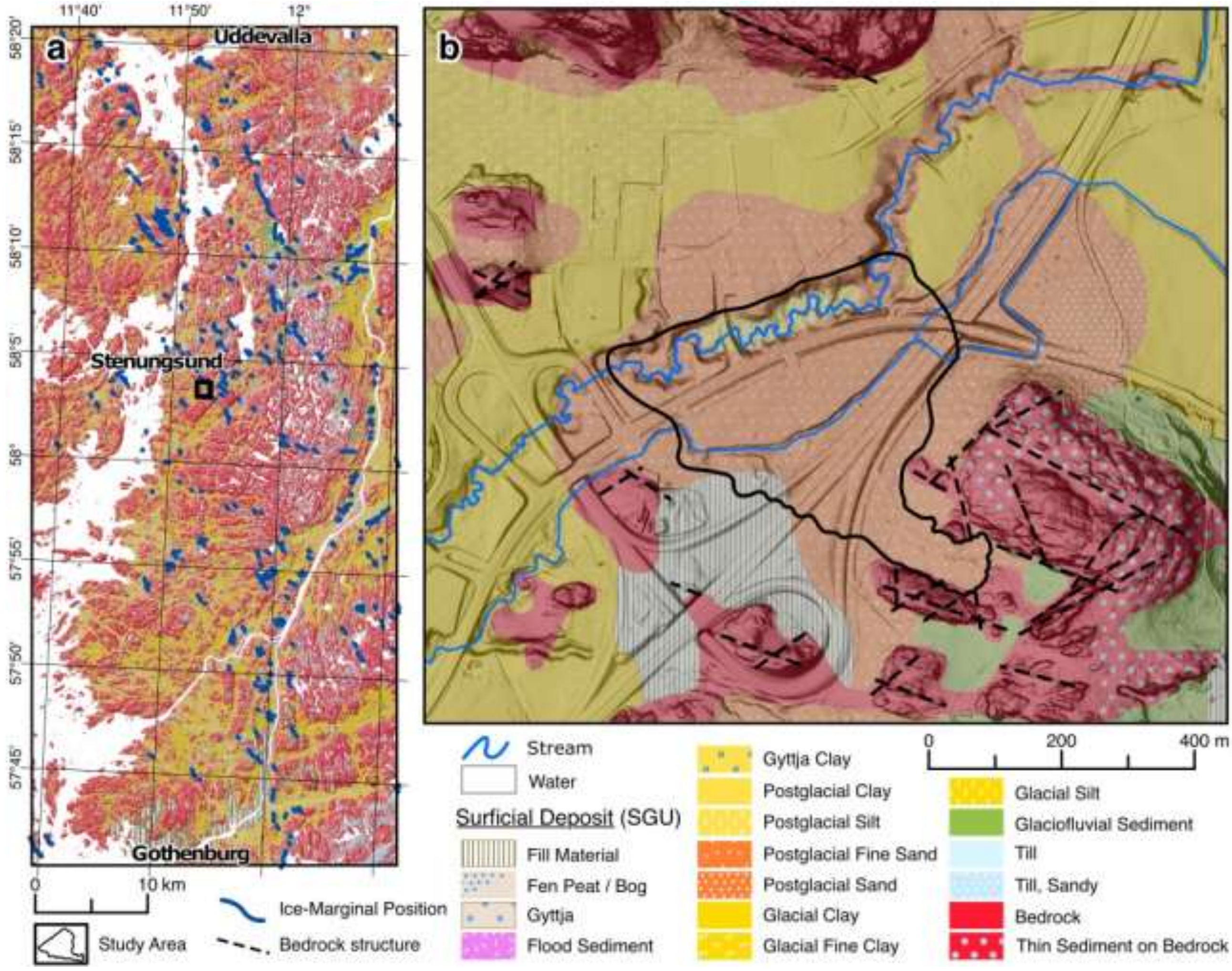

Fig. 2 **a** Regional geological setting where the Quaternary Deposit Map (SGU 2024) displays red for bare bedrock and yellow for clay. Blue lines represent ice-marginal positions (end moraines), and the black rectangle marks the extent of b. **b** The affected landslide area is zoomed in on the same surficial deposit map. Linear structures are marked on the bare bedrock. Postglacial silt and sand, wave-washed sediment during regression, superpose the previously deposited clay that is found on the surface where no wave-washed material was deposited or preserved.

During the deglaciation at the site, the ice margin readvanced and left a large glaciofluvial deposit just on and behind the hill, east of the landslide (Fig. 2). Regression later exposed these sediments to wave washing, reworking, and subsequent redeposition. As a result, the valley infill comprises interlayered glaciomarine clay, glaciofluvial outwash, and postglacial clay, silt, and sand with varying permeability.

Overall, the geological and geomorphological setting of Stenungsund combines several factors that predispose the area to landslides: fractured crystalline bedrock, thick valley-fill sediments dominated by glaciomarine clay, and geomorphological evidence of repeated glacial readvances and a marine environment. These features create conditions conducive to quick-clay formation, particularly when combined with hydrological fluctuations. Historically, until 1988, when construction of the E6 commenced, the area was an agricultural landscape.

Data and methods

Remote sensing

Multi-temporal airborne and drone LiDAR-derived digital terrain- and surface models (DTMs/DSMs; 2011–2024), orthophotos (1931–2024), and Sentinel1/2 imagery were used to quantify pre-event ground modifications and post-event changes. Spatial data were processed in ETRS89 UTM zone 33N (SWEREF99 TM) using standard GIS workflows; volumes were estimated by DEM differencing and cut–fill analysis. Dataset details and processing steps are summarized in Online Resource 1.

Kinematic analysis

By comparing pre- and post-landslide images, indications of ground movement can be identified. Objects visible in photographs allow for the measurement of displacement, while post-landslide surface morphology indicates the relative motion of different areas. Fissure patterns and material accumulation provide further insights into movement processes. These were mapped using orthorectified aerial photographs and LiDAR-based elevation models from Lantmäteriet (The Swedish mapping, cadastral and land registration authority.), as well as Google Street View (n.d.). These datasets were compared with post-slide photographs, photogrammetry, and DEMs.

Field mapping

C. Öhrling visited the site the morning after the event and subsequently conducted field investigations on approximately 20 occasions. Work included systematic ground photography and drone surveys to document morphology and structures. Several sections were cleaned and examined, supported by hand augering, sounding, and machine excavation. More than 50 samples were collected for lithological characterization and paleoenvironmental interpretation.

Hydrogeology & hydrology

No groundwater measurements were available at Stenungsund prior to the landslide, preventing direct assessment of pore-water pressure. However, data from the Geological Survey of Sweden (SGU) allow for the assessment of relative conditions, such as unusually high or rapidly changing levels (Hjerne et al. 2024). Most SGU stations represent natural, undisturbed settings, and those nearest to the region are distant and may reflect different ground conditions and weather patterns. To address this, SGU models groundwater levels for small aquifers using the Swedish Meteorological and Hydrological Institute (SMHI) weather data, which represents generalized till in recharge areas. These estimates are expressed as a unitless saturation index (0–100), where 0 and 100 correspond to the lowest and highest levels since 1961.

The SAGA GIS (Conrad et al. 2015) hydrology toolbox was used to assess changes caused by surface modification. Flow accumulation was calculated using the *Multiple Flow Direction* method (Freeman 1991; Quinn et al. 1991).

Geotechnology

Geotechnical documentation from the construction of the E6 provides important baseline information for the area (Lindmark and Norder 1988). The section passing Stenungsund was inaugurated in 1991. Several subsequent investigations during construction further characterized local sediment and stability conditions. Following the landslide, comprehensive geotechnical studies were undertaken during reconstruction, including detailed subsurface profiling and sampling (Berling 2024). These datasets collectively offer essential context for interpreting pre-failure conditions and post-event changes.

The landslide investigation was supported by the Norwegian Geotechnical Institute (NGI), which used finite element modeling (FEM) in Plaxis 2D (Bentley Systems 2023) with the NGI-ADPSoft material model (developed by NGI) to simulate the strain-softening (brittle) behavior of sensitive clays (Fornes 2024). The model analyzed a 5-stage driving mass (filling material) placed over sand and dry crust, superposing sensitive clay layers. To build all fill stages in the simulation, peak strengths were factored by 1.2–1.6 to account for 3D effects and sample quality, with residual strength set at one percent of peak active strength. The modeling identified the construction as the likely trigger, indicating that the natural slope had low capacity relative to the fill weight. The simulation replicated a horizontal progressive failure propagating through the sensitive clay, consistent with observed field conditions.

Other data

Radar imagery from SMHI and streamflow data from the Water Information System Sweden (VISS) were utilized to evaluate rainfall intensity and distribution. Sentinel-1-based Interferometric Synthetic Aperture Radar (InSAR) data were mainly used for analyzing ground settlements. This data was acquired from the Copernicus Land Monitoring Service (CLMS) through the European Ground Motion Service (EGMS). Additionally, seismic data from the Swedish National Seismic Network were collected to identify the landslide signal and distinguish it from other sources, such as mining and construction blasts.

Results

Pre-failure setting

Drone photographs captured on 20 September 2023 by freelance journalist Mikael Berglund were processed in ShapeMetriX 3D (3GSM GmbH, Austria) to reconstruct a 3D model depicting essential parts of the area as it appeared two days prior to the event. These data were aligned with pre-landslide DTMs—including the 2021 LiDAR dataset within the landslide area—and with post-landslide LiDAR surveys from the surrounding zone. This integration produced a composite DTM representing the topography as of 20 September 2023 (see Online Resource 2).

Surface elevation changes are presented as the difference in meters between two digital elevation models. To assess terrain modifications in recent years, comparisons were made for 2011, 2016, 2018, 2021, and 2023, representing conditions before the event.

Figure 3a shows elevation differences between 2011 and 2021, during which the gas station, fast-food restaurant, and hardware store were established (after 2016). Throughout this 10-year time span, progressive subsidence of the E6 roadway is apparent, not taking maintenance work and resurfacing into consideration.

InSAR time-series since 2014 reveal significant vertical deformation along the landslide-affected section of the E6, with average subsidence rates exceeding 5 mm yr^{-1} and localized settlements reaching over 20 mm yr^{-1} between 2015 and 2023. EGMS ORTHO data (03/08/2019–09/19/2023) indicate limited horizontal displacement (3 mm yr^{-1}) but substantial vertical settlement, although interpretation is constrained by coarse spatial resolution and uncertainty in horizontal motion estimates. The highest vertical displacement zones averaged approximately 17 mm yr^{-1} before failure, implying cumulative subsidence potentially exceeding 1 m since road construction in 1992 when accounting for repeated resurfacing works and glacial isostatic adjustment (GIA). These observations are consistent with long-term road monitoring data and previously projected settlement magnitudes from the original design studies.

When the E6 was built, Kärrbäcken and Ucklumsvägen were rerouted, and the associated channels/ditches were filled in (Lindmark and Norder 1988). In 2023, the construction of the area east of the E6 began, as well as modifications to the area immediately to the west (Fig. 3b). These operations included the removal of material from the slope adjacent to the southbound E6 exit ramp and the placement of fill at the top of the eastern slope.

The ground modifications also altered precipitation-runoff patterns and groundwater conditions. Figure 3c displays the runoff pattern in 2011, based on flow-accumulation modeling, while Figure 3d shows the runoff modelled from the the composite 09/20/2023 DTM. The flow-accumulation models indicate substantial changes in water pathways following the changes in the eastern area. The following refers to Figure 3d and the numbers in Figure 3b. First, the fill in the southern parallel valley (**1**), together with adjacent working roads and excavations south–southeast of the site, diverted runoff northward toward the future landslide. Similarly, blasting of bedrock to construct a working road directly south of the landslide pit (**2**) further increased runoff entering the depression. Farther east, at the hilltop, a small peatland was excavated and replaced with compacted fill to create a parking area (**3**). This change facilitated rapid surface runoff and likely increased the westward flow. In addition, gravel was excavated at the foot of the bedrock slope facing the future landslide (**4**), unintentionally creating an infiltration basin for groundwater. The final and most substantial modification was the large fill that later collapsed (**5**). This was built up between two bedrock shoulders, with retaining walls made of boulders and fillings of varying properties.

The various anthropogenic interventions in the natural environment surrounding the Stenungsund landslide area, including deforestation, excavation, and filling, affected groundwater and runoff conditions over a relatively short period prior to failure. The general groundwater model from SGU did not reveal anything abnormal during 2023; similar trends can be found in previous years. However, the construction works likely led to an abnormal situation. Witness accounts and surveillance footage indicate intense rainfall and extremely poor visibility during the landslide event. (SHK 2025). According to a meteorologist at SMHI, approximately 10–15 mm of rainfall likely fell locally around midnight over a duration of 1–2 hours and was classified as intense rainfall (Moran 2023). Radar imagery from SMHI suggests even higher intensities, which are further elaborated in the *Discussion*. Old pore-water pressure measurements in the valley record artesian groundwater (Lindmark and Norder 1988).

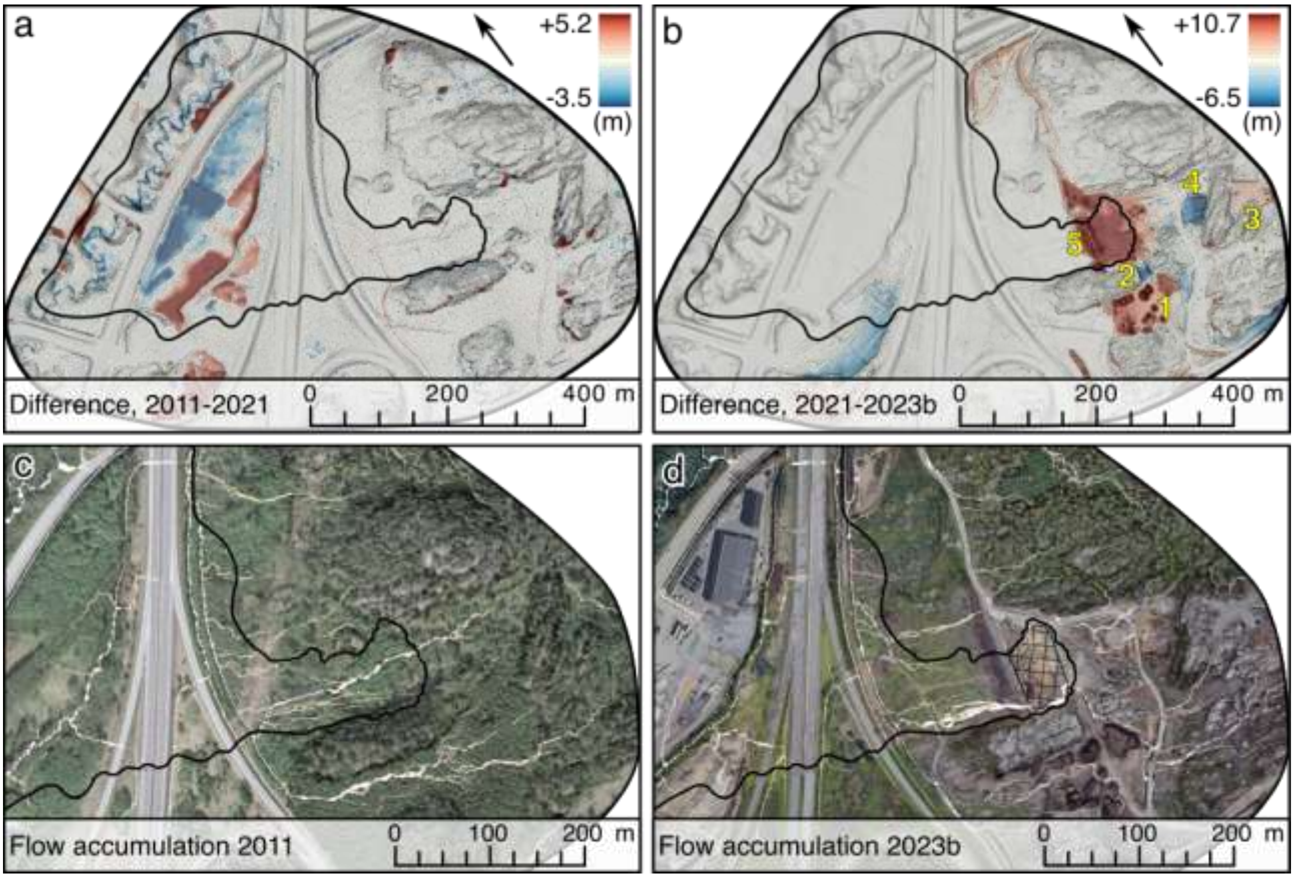

Fig. 3 Elevation difference between DTMs from **a** 2011 and 2021, and between **b** 2021 and 2023 before the event. Flow-accumulation models based on **c** 2011 DTM and **d** 2023 before the event. In 2016, the triangular (iron-shaped) area west of E6 started to develop. In 2023, until the landslide, the area immediately west of the E6 and the area east of it were developed. The interventions in the eastern part significantly affected the runoff. A large part of the natural path through the southern fracture valley was rerouted towards the landslide valley. Excavations of outwash material created groundwater infiltration basins.

Failure morphology

The landslide area is 15 ha, with a distance of 620 m from the back scarp to the slide masses in the river *Norumsån* ('Norumsån' from here on) and a width along the local road *Ucklumsvägen* of 450 m, while being 400 m parallel to E6 (Fig. 1). The elevation difference in the affected area is 37 m, between the top of the filling in the east at 72 m a.s.l. and the bottom of Norumsån in the west at 35 m a.s.l.

The vertical difference between the DTMs before (composite) and after the failure shows that displacement within the landslide pit reached approximately 20 m in depth, of which roughly half consisted of original deposits and half of fill material (Fig. 4). The profiles in the diagram represent elevation changes along the blue line in Figure 4. The bedrock surface is an approximation based on the available depth data.

The differential models also provide erosion and accumulation volumes of the failure masses relative to the pre-failure ground surface. It is difficult to interpret the actual failure surfaces from the geotechnical data, likely due to the high sensitivity of the clay above and below. However, based on the interpretation of vague indications from the CPTu and the knowledge of pilings in the northern area, it is possible to estimate various depths, ranging from 9 to 25 m in different areas. An interpolated model ('kriging') of the slip surface was also constructed from the CPTu interpretations and then used to calculate the volume between that and the pre-landslide DTM (see Online Resource 3 and 4). There are problems

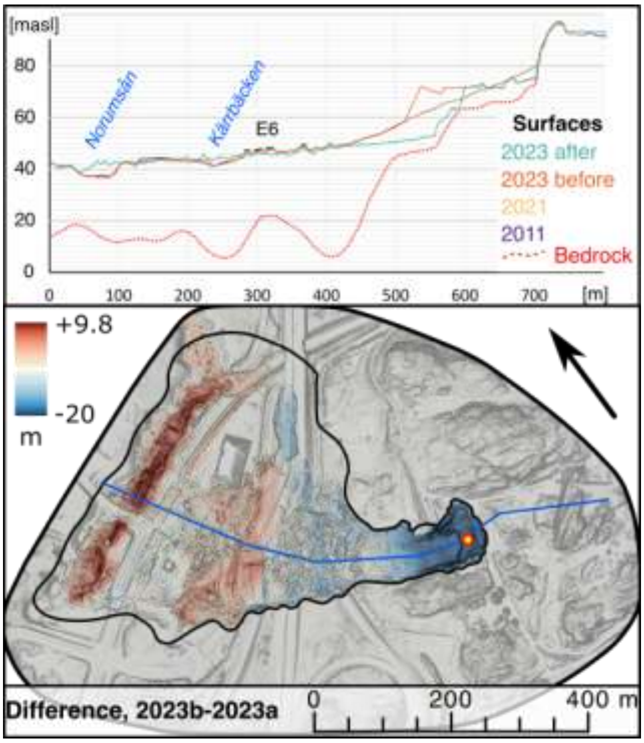

Fig. 4 Elevation profiles from generations of LiDAR images and a modeled bedrock surface. The blue line on the map represents the location of the profiles. The map shows the elevation difference between DTM_230920 and DTM_231106. A yellow-red star marks the shelf of clay that remained after the event.

with both methods, i.e., the adoption of cubic volumes and edge effects. We therefore estimate the volume of displaced masses amounts to 1.2–1.85 million m^3 (see Online Resource 3).

In the central part of the area, the E6 shifted approximately 50 m westward, producing an initial subsidence followed by a heave. Farther west, in Norumsån, the kinetic energy of the slide dissipated, and displaced clay dammed the river. The northern segment of the E6 involved in the event moved primarily in the vertical direction, behaving almost like a sinkhole. This collapse, together with the northernmost heave affecting the local road (*Ucklumsvägen*), represents the most complex deformation patterns associated with the landslide. These features are discussed further in subsection *Kinematics & deformation mapping*.

Sedimentological/geotechnical findings

The failed mass is dominated by thick clay deposits overlying a thin frictional layer. Although stratigraphic data were initially lacking, later stabilization works in the eastern parts exposed clear sections east of the landslide scarp. These exposures, in addition to those revealed by the landslide, show the natural ground surface beneath 3–10 m of anthropogenic fill composed of gravel, marine clay with shell fragments, sand, and macadam.

Underlying sediments consist of glaciofluvial subaqueous fan deposits, with cyclic bedding of silt, sand, and gravel. These interbedded layers form hydraulically conductive horizons that influence groundwater flow. Intact clay inside the landslide scarp (see star in Fig. 4) is at least 5 m thick and contains multiple silt–sand and shell-rich layers. The clay exhibits vertical fracturing with sand-filled millimeter-scale fissures at depths where desiccation is unlikely, interpreted as compaction-related fracturing (c.f. Brodzikowski 1981) that enhances permeability and may promote pore-water pressure increase and quick-clay development.

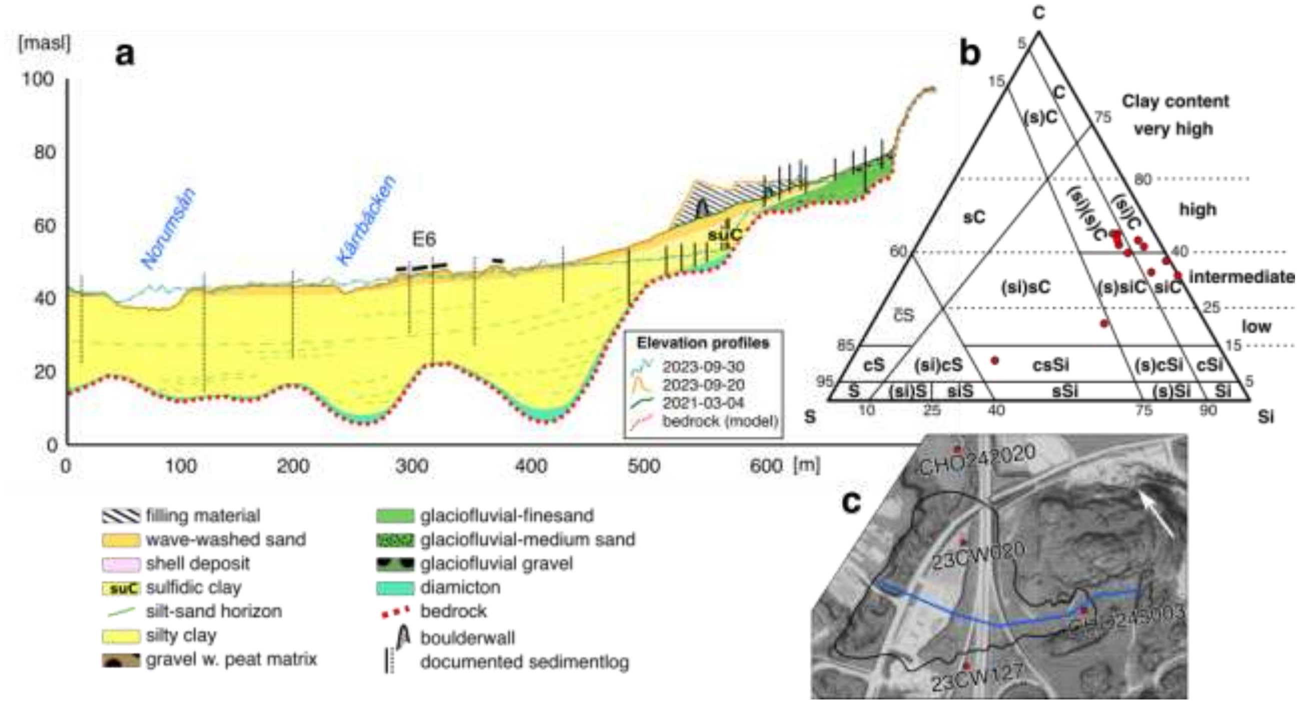

Fig. 5 (**a**)Mapped and interpreted stratigraphy along the blue line in **c**, where the location of the boreholes is marked with red circles. The landslide area is represented by the black polygon. **b** Grain-size plot (after Stevens 1983) with the mentioned samples from boreholes.

A profile along the E6 corridor (Lindmark and Norder 1988) and later post-landslide drillings (Berling 2024) correspond well with our observations. The clay thickness is around 10 to 15 m in the southern parts and increases northward to 40 m within the landslide area, continuing to increase further northward. In borehole 23CW127 (Fig. 5c), piston samples from 4–15 m depth show alternating gyttja-rich silty clay, silt-rich clay, and clayey silt with sand layers. Borehole 23CW020 (6–34 m) contains gyttja-rich silty clay to 26 m, followed by sand and gyttja-bearing silty sand and silt. Samples with low clay content and higher sand content in Fig. 5b are from 23CW020 at 28 and 30 m depth. The remaining samples are closely plotted as silty clay to clay, with 31 to 50% clay. Gyttja-rich clay occurs at notable depths, and freshly remoulded clay emitted sulphide odours and contained shell fragments.

Table 1 presents the boreholes where piston-core samples have been analyzed with a focus on strength properties. The depth interval for quick clay should be considered with caution, since samples have not been collected for the complete probing depths. The old samples ('86WWxxx') were aimed at the upper 15–20 meters, hence there is likely deeper quick clay at some of those locations. All but two locations are categorized as quick clay according to the Norwegian definition (sensitivity ≥ 30 and remolded undrained shear strength less than 0.5). One additional location is removed if the Swedish definition is used ($S_t \geq 50$ and $\tau_R < 0.4$).

Kinematics & deformation mapping

Gravel roads, E6 and Ucklumsvägen, guardrails, fences, light poles, culverts, buildings, prominent trees, and similar objects were mapped in the before and after images. Road markings that had not been repainted between the most recent pre-slide orthophotos and the new post-slide imagery also provided valuable constraints (Fig. 6a). The displacement vectors clearly illustrate the magnitude and direction of ground displacement (Fig. 6b). Material from the eastern embankment was identified almost 160 m west of its original position, representing the largest horizontal

Table 1 Boreholes where piston samples have been analyzed with respect to shear strength and sensitivity. XY coordinates are in ETRS89 UTM Zone 33N. Quick clay is categorized by the Swedish (QCSwe) and Norwegian (QCNor) definitions. Max, min, and average sensitivity represent all measured values, not only the QC ones.

BoreholeID	X	Y	Depth	QCSwe	QCNor	QC depth	Smax	Smin	Savg
23CW013	316088	6439594	23	QC	QC	6.0–23.0	384	42	213
23CW020	316098	6439706	34	QC	QC	12.0–34.0	373	29	133
23CW026	315974	6439498	14	QC	QC	6.0–14.0	194	26	100
23CW035B	315903	6439559	14	QC	QC	5.0–13.0	92	25	69
23CW051	316208	6439724	29	QC	QC	8.0–29.0	444	108	293
23CW052	316106	6439650	24	QC	QC	9.0–42.0	410	88	264
23CW088	316034	6439508	16	QC	QC	13.0–16.0	158	27	89
23CW127	315909	6439472	15	QC	QC	4.0–14.0	164	31	117
23CW156	315851	6439509	11	QC	QC	3.0–11.0	112	35	67
23CW169	316127	6439408	10		QC	8.5–9.5	68	27	44
23CW170	316166	6439413	6				40	32	45
23W002	315700	6439744	18	QC	QC	5.0–15.0	421	48	195
23W006	315801	6439759	15	QC	QC	8.0–15.0	372	24	260
23W013	316051	6439862	25	QC	QC	6.0–25.0	169	50	93
23W014	315921	6439775	25.2	QC	QC	6.0–25.2	211	41	104
23W017	315788	6439655	20	QC	QC	4.0–20.0	421	37	249
23W024	315920	6439713	22	QC	QC	7.0–22.0	210	91	150
23W027	315985	6439736	22	QC	QC	9.0–22.0	201	56	96
23W031	316079	6439757	32	QC	QC	22.0–32.0	206	31	63
SW2323	315984	6439443	18				34	1	18
SW2330	315895	6439432	12	QC	QC	10.0–12.0	52	3	28
E15-EQC21	315945	6439686	18	QC	QC	4.0–18.0	124	5	76
86VV530	316191	6439750	18.2	QC	QC	4.0–18.2	160	4	76
86VV534	316063	6439596	18	QC	QC	3.0–18.0	382	64	269
86VV537	315972	6439491	13	QC	QC	4.0–12.0	271	17	110
86VV538	316154	6439704	20	QC	QC	4.0–20	491	79	322
86VV548	315917	6439736	16.2	QC	QC	3.2–16.2	420	27	232
86VV550	316076	6439779	16.2	QC	QC	2.2–16.2	64	39	54
86VV551	315579	6439589	17.2	QC	QC	2.2–17.0	317	22	192
86VV552	315641	6439675	16.2	QC	QC	3.2–16.2	338	7	213

movements in the area (see unit 0a–0b). In general, displacement decreases from east to west and north. Minor retrogressive failures along the primary scarp generated shorter movements; for example, parts of the construction road at the back scarp of the slide (see unit 23) were displaced by approximately 15 m.

Mapping fissures and the morphology of displaced masses, on post imagery, provides further insight into deformation patterns. The mapped structures reflect the kinematics (Fig. 6c): lobes indicate motion perpendicular to their fronts, while fractures may form extensional, compressional, or sheared patterns depending on the directions of the forces. Therefore, these features can be used to reconstruct the movement pattern. Cross-cutting relationships are observable within these structures, and several major examples are highlighted with arrows representing relative movements in Figure 6d. Both orthophotographs and field observations document tensional and compressional structures, as well as horizontal shear components (including several examples of echelon fractures). In addition, sliding fissures on exposed blocks of clay were mapped and used as indications of local movements, for example, along lobes (which were found to be orientated normal to those). The color codes in Figure 6d represent surfaces with internally consistent deformation or other common characteristics, and these are referenced in the following sections.

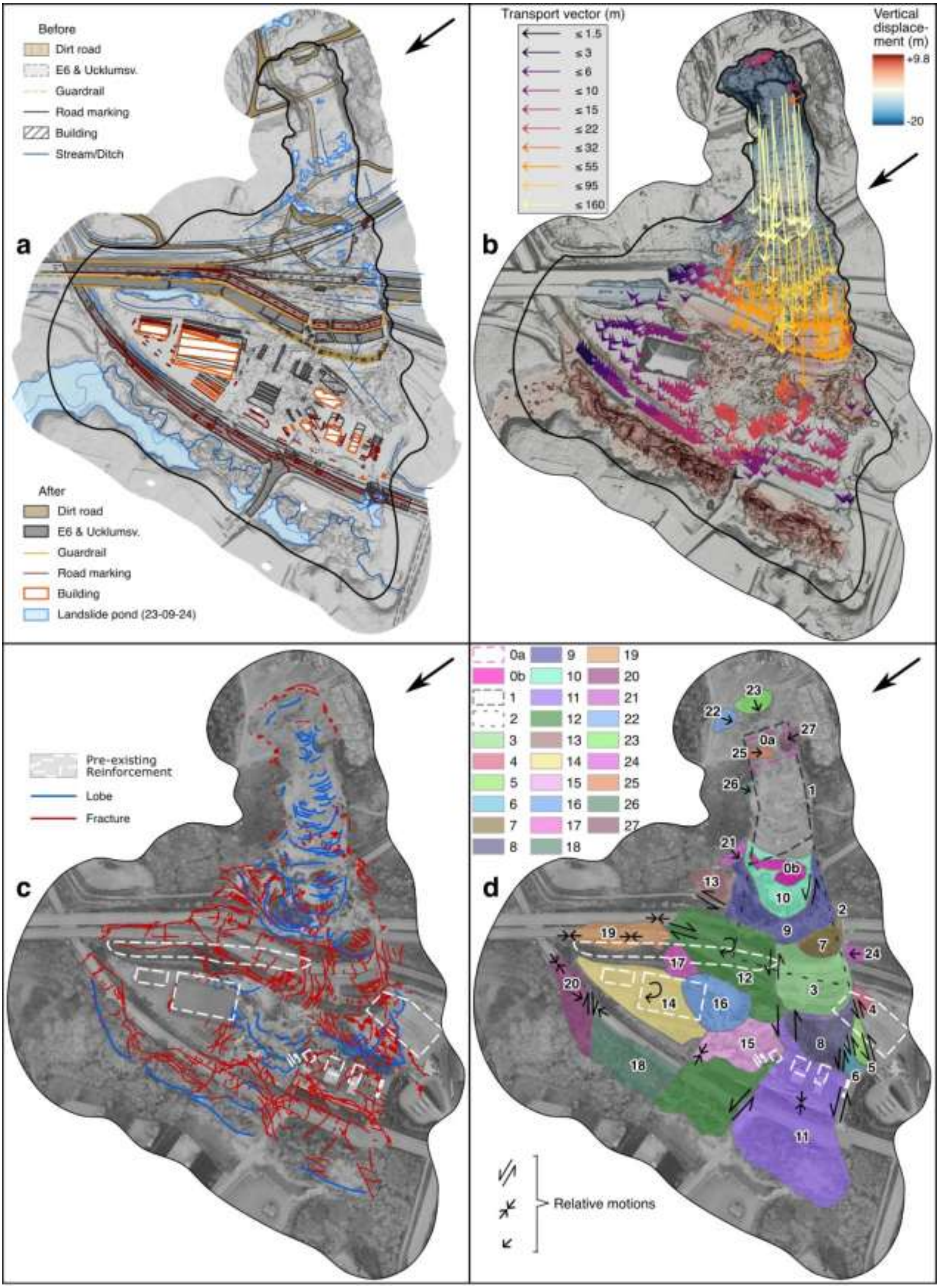

Fig. 6 a) Ground displacements associated with the landslide were mapped using multiple identifiable physical objects, and the impoundments formed by the event were subsequently documented. b) Vectors were created from identified objects in pre- and post-failure images. Transportation of material was up to 160 m in the erosional eastern parts and then decreased towards Norums˚an. c) Landslide-surface morphology shows lobes of material and fissures; these can be used to further interpret the progression. d) The landslide was subdivided into 27 morphological units for easier reference. Relative movements within the slide masses are marked by arrows. White-dashed lines mark where reinforcements were present before the event; embankment along E6 and piled surfaces below buildings and fuel tanks. Background: Hillshading and orthophoto derives from post-failure LiDAR acquired by Swescan on 11/06/2023.

Event chronology

Data from the district heating system shows a pressure drop at 01:23 a.m., and at 01:40, the main pipeline ruptured. Between 01:35 and 01:40 a.m., a sharp increase in flow was recorded at the wastewater pump station southwest of the gas station.

Information from the power grid shows that line relays tripped at 01:40:30 and 01:40:40 a.m. (SHK 2025). A seismic signal interpreted as the landslide was detected between 01:39:30 and 01:41:20 a.m., reaching its maximum amplitude at 01:40:10 a.m. Surveillance footage reveals that a car entered the landslide area on Ucklumsvägen heading northeast at 01:40:08 a.m. When emergency responders arrived on this road from the northeast, they met a person who reported driving along the road when the streetlights went out and feeling the car jolt when passing the hardware store—the location of the significant uplift in Ucklumsvägen.

At approximately 02:10 a.m., rescue personnel positioned in the southern part of the area heard loud rumbling noises from the eastern portion of the landslide zone. This prompted them to evacuate the area along with individuals extracted from their vehicles.

A truck driver, who is also a trained geologist, reported that a couple of days before the landslide, subsidence and water-eroded channels up to half a meter deep and wide appeared in the construction roads above the future slide. Photographs from two days before the event show signs of erosion and soil movement in the filling embankment. Cracks indicating further movement are also visible. Analysis of the elevation levels in the photographs (06/20/2023) reveals possible settlement across the entire embankment.

Subsidence and erosion of the construction roads east of the embankment indicate settlement-sensitive ground and water erosion. However, such deformations are not uncommon on construction sites with frequent heavy-truck traffic. Pre-event photographs show erosion and cracking in the embankment and construction roads, suggesting localized instability and permeability within the fill.

A motorist driving northbound on the E6 around 10 p.m. the evening before the slide perceived the road surface as deformed and wavy. Another witness, travelling southbound on the E6 around 01:00 a.m., reported "bumps" in the road passing the fast-food restaurant. During the evening before the event, witnesses observed unusually high water flow in Kärrbäcken and Norumsån.

The reported anomalous road deformation and water flow in the hours preceding failure are consistent with the instrumental timeline. Witness accounts of unusual phenomena around 10 p.m. and 01 a.m. are noteworthy because they can be reconciled with the hard data described above. Similar sequences for *translational progressive landslides* have been reported (Hutchinson 1961; Bjerrum 1967; Locat et al. 2011; Quinn et al. 2012; Torrance 2012; Hungr et al. 2014; Bernander et al. 2016).

It is thus established that the landslide occurred shortly before 01:40 a.m. and caused intense ground movements lasting several minutes. The seismic signal probably reflects the duration of vibrations generated by the mass movements;no alternative explanation for this signal has been identified. Morphological and kinematic analyses of the displaced masses do not provide an exact timestamp but do reveal the relative sequence of movements.

The following is a proposed interpretation of the sequence of events (Fig. 7), initially based on morphology and stratigraphy, integrating all observations and time constraints. This interpretation is consistent with and supported by the FEM results (Fornes 2024), lending additional confidence to the proposed sequence.

Panel **a** illustrates approximately where the initial failure in the underlying clay layers occurred. This may not correspond to the first perceptible surface movement; the failure could have propagated along the modelled slip surface, over ten meters below ground. Panel **b** shows this propagation reaching the near-surface zone, where the foundation and weight of E6 provide and/or the bedrock morphology resisting forces. Settlement occurs in the fill material while uplift develops farther downslope. This uplift may have caused the deformation experienced in the E6 surface. Drainage in this area would also have been affected, potentially altering flow in Kärrbäcken. Panel **c** shows the structural failure of E6; once the resisting forces are lost (and the clay remoulds), the translational(-progressive) block—already weakened by overloading in the east—follows. A succession of mass movements then occurs, ultimately reaching equilibrium as material is displaced into the floodplain of Norumsån. The mass movements that occurred during this landslide precursor phase likely created the recorded seismic signal. The seismic signal may have been amplified by structural failure of the comparatively rigid E6 roadway. Smaller retrogressive failures continued locally after the main event, with the larger ones occurring farthest east (Panel **d**). One of these may have caused the loud noise at 02:10 a.m. that prompted the emergency services to withdraw; this may, for example, have been the collapse of the construction road at the far eastern extent of the slide. Orthophotos show that units **25**, **26**, and **27** failed two to three days later (Fig. 6d).

Discussion

Mechanisms: interplay of geology, hydrology, and human triggers

The geological history of the area has created favorable conditions for the formation of quick clay. The nearby position of the active ice margin resulted in a varied proglacial stratigraphy with coarser (siltier and sandier) beds, creating strong hydrological connectivity to the valley's extensive clay deposits. Bedrock exposed above the water-bearing sediments further enhances the potential for infiltration along the weathered and fractured bedrock surfaces. Shell-bearing layers can be traced throughout the area, creating a hydrological connection between the glaciofluvial sand in the east and the upper clay deposits in the west. As glacial rebound exposed the slopes to wave action, mainly silt and sand were washed and transported downslope, forming inter-fingering deposits within the clay. Groundwater flowing along these pathways into sediments overlain by clay can generate high pore-water pressures, producing artesian groundwater within the valley. The movement of water through the clay facilitates leaching processes and the development of quick clay.

Near the landslide scar, on the flanks of protruding bedrock, clayey shell-rich sediments are locally observed resting directly on the bedrock surface. However, coarser sediment deposits are present in depressions and fracture zones.

This implies that precipitation falling on elevated areas can infiltrate the soil layers and percolate downward into and beneath the clay deposits.

The anthropogenic development of the eastern part of the area significantly changed the runoff pattern (Fig. 3c & d). When the fill material was placed in the southern fracture valley (#1 in Fig. 3b) together with excavations and roads, a significant part of the runoff was forced north to the valley of the landslide. In addition, the blasting of the bedrock to create a road (#2 in Fig. 3b) further increased the possibility of directing runoff to the north.

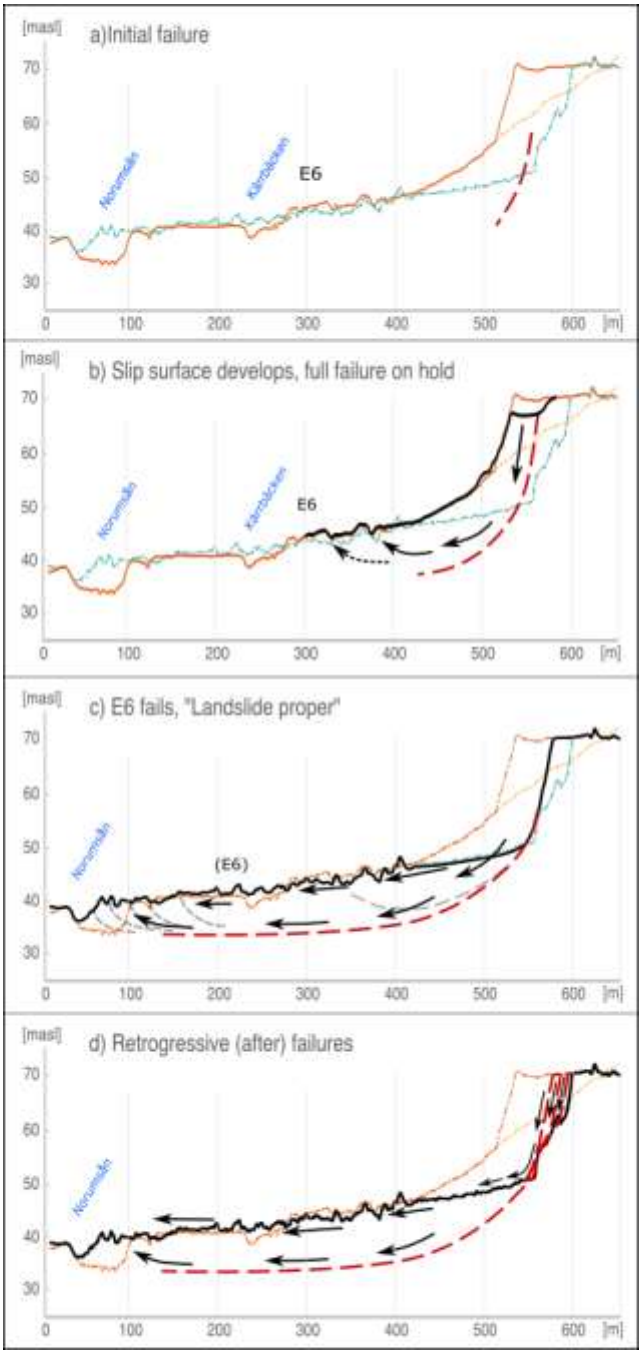

Fig. 7 Suggested sequence of events for the landslide. Based on failure modeling (Fornes 2024) and morphology and kinematic mapping. **a**. The loading causes the soil layers under the 'bank' (anthropogenic fill) to begin developing failures. **b**. The failure continues according to the theory in a translational progressive landslide. **c**. When E6 fails, and its resisting force disappears, the failure surface of the slab landslide is probably well-developed. **d**. The landslide develops progressively, with a spread to Norumsån and northwards. Up to 10 m heave in Norumsån. The furthest parts east, at the rear edge of the landslide, fail regressively.

As indicated above, the varied stratigraphy, as well as the human development of the site, allowed groundwater pressure to increase within the clays. The general groundwater model from SGU showed increasing levels when the landslide occurred. However, not stronger than in previous years, which indicates that the altered ground conditions were likely the differentiating factor.. In addition, intense rainfall in the hours before the event likely increased pore-water pressures. Considering the southwesterly winds at the time, the radar image in Figure 8 suggests extreme precipitation locally (> 100 mm/h), which is mutually consistent with witness accounts. Further, artesian pressures, which were known to occur at the bottom of the valley, developed as a result of groundwater pathways along permeable layers.

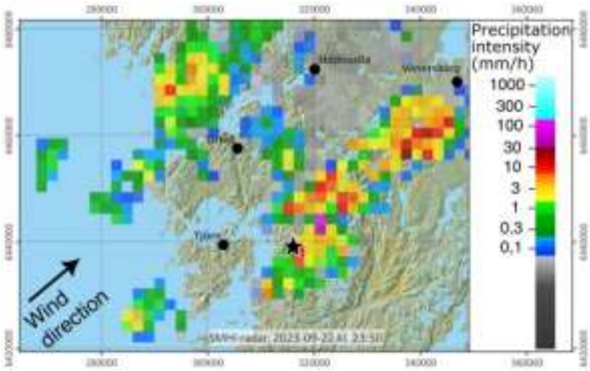

Fig. 8 Meteorological radar image presenting precipitation at 11:50 pm, less than two hours before the event. The black star marks the location of the Stenungsund landslide. Note the wind direction and the purple cells that represent up to more than 100 mm/h. Downloaded (and modified) from https://www.smhi.se/data/nederbord-och-fuktighet/nederbord/radarbilder-aktuella-och-historiska.

Construction activities, including filling, excavation, and foundation works, altered the natural balance of the valley. Over the past 35 years, several developments have affected the area. During the last months preceding the landslide, the slope to the east was also developed. When the mass balance of the ground changes, sediment layers may adapt to increased loading through consolidation. The addition of fill material in the eastern part of the area occurred relatively quickly, which likely resulted in the underlying layers not consolidating at the same rate. However, consolidation effects were also considered contrastinglyduring calibration of the FEM model. The removal of sand and gravel upslope along the bedrock high possibly increased mass-balance stability. At the same time, as mentioned above, this created conditions for increased groundwater infiltration and pore-water pressure buildup. Furthermore, it was observed that the fill contained a significant amount of water, which also would negatively influence the consolidation process.

InSAR data show that the E6 had significant ongoing subsidence. The highway area is principally flat, and the consolidation of clay is therefore not considered a weakening factor, but rather a stabilizing. Rerouting and filling of Kärrbäcken when the E6 was built, together with the ditches along the old Ucklumsvägen during the construction of the E6, may partly explain the unusual ground movements observed in the northern part of the landslide area. These movements occurred when the mass balance in other parts of the area changed; there is no evidence that the landslide was initiated there. Several well-founded structures in other parts of the landslide zone likely influenced how the ground moved during the event (see Fig. 6c & d).

Although land use and the cumulative changes in mass balance within the valley have negatively affected ground stability, the results of the investigation strongly suggest that the weight of the fill operations in the east caused the failure.

Interpretation of the failure progression

In general, the initial failure is interpreted to have been caused by the loading of the fill, which exceeded the strength of the underlying sediments. Elevated pore-water pressures likely influenced the timing of the failure. The areal extent of the landslide was constrained by the bedrock structures, the cut-down floodplain (Norumsån), and the presence of quick clay. The eastern bedrock shoulders channeled the initial movement, while the southern fault-line scarp controlled its straight alignment. Lower in the valley, bedrock blocks to the north created conditions for increasing clay thickness—and thus quick-clay thickness—which enabled the landslide progression to turn in that direction (see Online Resource 4).

More specifically, the initial failure occurred beneath the fill, possibly parallel to a coarse-grained layer that developed an extensive slip surface. This triggered a translational(-progressive) block slide with settlement in the fill embankment, followed by heave that developed up to 250 m farther downslope, at E6 (see **0a** in Fig. 6d). When resistance at E6 failed, the quick clay rapidly mobilized in a dispersive manner, likely along a partly already developed slip surface. The translational progressive block moved into position **0b**, enabled by the stepwise removal of material to the WNW (**4, 3, 5, 6, 8, 11, 12**). The stability berm on the northern part of E6 (see dashed white markings) provided greater resistance, pushing material toward the ENE (**13**), inducing a rotational movement of E6 (**12**), and generating a general force directed ENE along E6 (see compressive relative motion). The recorded seismic signal likely represents the massive movements that followed when E6 broke.

When forces reached Norumsån, the perpendicularly orientated Sylvägen (Fig. 1) likely acted as a counterforce, primarily, redirecting the kinetic movement northward (**18**). In addition, the greater depths of clay allowed movements in this direction, creating the horizontal "rotation" of the hardware store (**14**).

The clay blocks that surfaced in Norumsån show indications of circular-cylindrical slip surfaces. The blocky appearance is also indicative of late movement in opposition to initial failure.

The material from the collapse of E6 at (**19**) does not visually present a natural escape, indicating that space was created underground. The general movements suggest that it was forced under the piled hardware store in a circular-cylindrical manner. This movement of material may have interacted with the kinetic movement from Sylvägen and contributed to the uplifted fault in Ucklumsvägen (**20**).

Several small retrogressive failures along the back scarp followed the main event (**21**, **22**, **23**). Two to three days later, units **25**, **26**, and **27** failed.

Scandinavian quick-clay landslides

Sensitive-clay landslides are recurrent in Scandinavia and are evident in geomorphology and historical records. High-impact cases are frequently linked to human activities (Tab. 2). The Surte and Tuve cases provide close analogues for translational–progressive failure and retrogression (Bernander et al. 2016). In Surte, the landslide also involved an initial failure confined/channeled by bedrock, extensive runout across flat terrain, infrastructure impact, secondary cylindrical failures progressing into a river, and pronounced retrogressive failure along the back scarp (Jakobson 1952).

Lessons for hazard assessment

The Stenungsund landslide exemplifies the critical importance of understanding both natural and human-induced triggers in quick-clay terrain. Groundwater fluctuations, compounded by fill placement and altered drainage, significantly reduce slope stability. The role of historical sedimentation patterns and valley geometry must also be acknowledged.

Table 2 Comparison with other high-sensitive clay landslides in Sweden and Norway. Area and runout are difficult to compare, especially between progressive and retrogressive types, as well as those terminating in water. The methodology also differs for volume calculations.

Event/ location	Year	Coun-try	Area (ha)	Volume (10^6 m^3)	Runout (m)	Failure mechanism	Anthropogenic trigger/cause	Fata-lities	Reference
Surte	1950	Swe	22	3	700	Translational progressive	Train vibrations, loading	1	Caldenius et al. (1956) Jakobson (1952)
Göta (Lilla Edet)	1957	Swe	32	3-5	300	Retrogressive flow	Factory area	3	Odenstad (1958)
Tuve	1977	Swe	27	3–4	800	Translational progressive failure	Housing area, Culverting, heavy rainfall	9	Hartlén 1984 Bernander et al. (2016)
Rissa	1978	Nor	36	2-6	1400	Retrogressive flow	Excavation/loading at shoreline	1	Gregersen (1981) Robson et al. (2022)
Småröd (Munkedal)	2006	Swe	8.5	—	450	Progressive	Construction + rainfall	0	SHK (2009)
Gjerdrum (Ask)	2020	Nor	38	1.35	2000	Retrogressive flow	non-mitigated long term creek bank erosion	10	Penna & Solberg (2021) Ryan et al. (2021)
Stenung-sund	2023	Swe	15	1.2-1.75	630	Translational progressive	Construction loading + rainfall	0	This study

Limitations and Future Work

Key limitations include (i) the lack of pre-event pore-water pressure measurements, (ii) uncertainty in local rainfall intensity, and (iii) constraints in modeling progressive failure. The multi photo DTM (Online Resource 2) was adjusted vertically by 2-4 m to align with surrounding LiDAR imagery, which leads to an approximate margin of error of 1 m. In this study, this is considered negligible. Future work should prioritize integrated borehole–geophysics interpretation, 3D stratigraphic/hydrogeological modeling, coupling these with progressive-failure FEM, as well as targeted geochemical/mineralogical analyses to explain geotechnical and sedimentological variability.

Conclusion

Quick-clay deposits in paleo-marine settings pose a latent risk, particularly under disturbed hydrological regimes. The 2023 Stenungsund landslide highlights the need for integrated geotechnical, geological, and hydrological assessments in land use planning. Improved risk mapping, monitoring, and public awareness are vital. The key findings of this study are as follows:

- The 23 September 2023 Stenungsund landslide was primarily triggered by anthropogenic fill from recent placement, which exceeded the strength of the underlying sensitive and locally quick clay.
- Thick marine clays interbedded with permeable silt, sand, and shell-rich layers created strong hydrogeological connectivity, promoting elevated pore-water pressures and clay sensitivity.
- Construction activities significantly modified surface topography and drainage, redirecting runoff and enhancing groundwater infiltration along fractured bedrock and permeable sediment horizons.
- Heavy rain in the days before and during the event likely contributed to the timing of the failure.
- The landslide evolved as a translational-progressive failure, with deep-seated initiation followed by rapid mobilization once the clay was remoulded, and a second phase involving circular-cylindrical failures.
- The Stenungsund case indicates that cumulative anthropogenic modification was a dominant factorin major quick-clay landslides and underscores the need for integrated geological, geotechnical, and hydrological assessments in infrastructure planning.

Supplementary Information:

The online version contains supplementary material available at https://doi.org/xxxyyyzzz

Acknowledgements

The authors gratefully acknowledge the Swedish Geological Survey (SGU), the Swedish Geotechnical Institute (SGI), and the Swedish Transport Administration (Trafikverket) for providing access to data and documentation relevant to this study. The authors also thank Mikael Berglund (journalist), Björn Lund (Swedish National Seismic Network), and John Dehls (Geological Survey of Norway). Cecilia Karlsson (SGU) assisted with the deep (>5 m) hand augering. Mark D. Johnson provided valuable comments that improved the language of the manuscript. Finally, we thank the anonymous reviewer who suggested several improvements.

Funding

This study was funded by the Swedish Accident Investigation Authority as part of the governmental investigation.

Author contribution

Christian Öhrling: Conceptualization; Investigation (work conducted in conjunction with the governmental Accident Investigation); Data curation; Formal analysis; Visualization; Writing – original draft. Ola Fredin: Conceptualization (selection of manuscript focus); Methodology; Writing – review & editing; Supervision. Christian Öhrling and Ola Fredin: Validation; Writing – review & editing.

Declarations

Conflict of interest The authors declare no competing interests.

Disclaimer The funders had no role in the design of the study; in the collection, analysis, or interpretation of data; in the writing of the manuscript; or in the decision to publish the results.

References

Bentley Systems (2023) Plaxis 2D. Finite element software for geotechnical analysis

Berling V (2024) Väg E6 Stenungsund Återuppbyggnad, Munkeröd 1:5 med flera - markteknisk undersökningsrapport (MUR) geoteknik : E6 Stenungsund – Reconstruction Report. COWI report 1G14MUR1, Trafikverket

Bernander S, Kullingsjö A, Gylland AS, et al (2016) Downhill progressive landslides in long natural slopes: triggering agents and landslide phases modeled with a finite difference method. Canadian Geotechnical Journal 53(10):1565–1582. https://doi.org/10.1139/cgj-2015-0651

Bjerrum L (1967) The Third Terzaghi Lectures; Progressive Failure in Slopes of Overconsolidated Plastic Clay and Clay Shales. Journal of the Soil Mechanics and Foundations Division 93(5):1–49. https://doi.org/10.1061/JSFEAQ.0001017

Brodzikowski K (1981) Dilatancy and the course of the deformational process in unconsolidated sediments. Annales Societatis Geologorum Poloniae 51(1-2):83–98

Caldenius C, Lundström R, Fellenius B, et al (1956) The Landslide at Surte on the River Göta Alv: a geologico-¨ geotechnical study. Geological Survey of Sweden (SGU) 27

Conrad O, Bechtel B, Bock M, et al (2015) System for Automated Geoscientific Analyses (SAGA) v. 2.1.4. Geoscientific Model Development 8(7):1991–2007. https://doi.org/10.5194/gmd-8-1991-2015

Fornes P (2024) Skredet i Stenungsund - progressiv bruddutveckling : The Landslide in Stenungsund – Progressive Failure Progression. NGI report 20230683-01-R, Norwegian Geotechnical Institute, NGI

Fred´en C (1987) Beskrivning till jordartskartan Marstrand NO/Göteborg NV: Description to the quaternary map Marstrand NO/Gothenburg NV. No. 63 in Ae, Geological Survey of Sweden (SGU), Uppsala

Freeman TG (1991) Calculating catchment area with divergent flow based on a regular grid. Computers & Geosciences 17(3):413–422. https://doi.org/10.1016/0098-3004(91)90048-I

Gregersen O (1981) The Quick Clay Landslide in Rissa, Norway: The Sliding Process and Discussion of Failure Modes. NGI Publication 135

Hartlén J (1984) Tuveskredet Slutrapport : Tuve Landslide Investigation Report. SGI report 11a, Swedish Geotechnical Institute (SGI), Linköping

Hjerne C, Retzner A, Hellstrand E, et al (2024) Klimatmodellering av grundvatten – grundläggande analys : Climate modeling of groundwater – basic analysis. SGU report 2024:04, Geological Survey of Sweden (SGU)

Hungr, O., Leroueil, S., & Picarelli, L. (2014). The Varnes classification of landslide types, an update. *Landslides*, *11*(2), 167–194. https://doi.org/10.1007/s10346-013-0436-y

Hutchinson, J. N. (1961). A Landslide on a Thin Layer of Quick Clay at Furre, Central Norway. *Géotechnique*, *11*(2), 69–94. https://doi.org/10.1680/geot.1961.11.2.69

Isacsson U, Sellin C, Thorén T, et al (2025) Skred vid Stenungsundsmotet i Stenungsunds kommun, Geoteknisk utredning av släntstabilitet : Landslide at Stenungsundsmotet in Stenungsund Municipality, Geotechnical investigation of slope stability. SGI report 20158, Swedish Geotechnical Institute (SGI), Linköping

Jakobson B (1952) Landslide at Surte on the Göta River. Swedish Geotechnical Institute (SGI), URL https://urn.kb.se/resolve? urn=urn:nbn:se:swedgeo:diva-347

Lidmar-Bergström K (1982) Pre-Quaternary geomorphological evolution in southern Fennoscandia. No. 785 in Serie C, Geological Survey of Sweden (SGU), Uppsala

Lidmar-Bergström K (1997) A Long-Term Perspective on Glacial Erosion. Earth Surface Processes and Landforms 22(March 1996):297–306. URL https://doi.org/10.1002/(SICI)1096-9837(199703)22:3%3C297::AID-ESP758%3E3. 0.CO;2-R

Lindmark A, Norder BE (1988) Väg E6 Göteborg - Uddevalla, anläggning av motorväg på delen Stora Höga Bratteröd : Road E6 Gothenburg - Uddevalla, construction of motorway on the Stora Höga Bratteröd section. Bygghandling 196, Swedish Geotechnical Institute (SGI), Gothenburg

Locat A, Leroueil S, Bernander S, et al (2011) Progressive failures in eastern Canadian and Scandinavian sensitive clays. Canadian Geotechnical Journal 48(11):1696–1712. https://doi.org/10.1139/t11-059

Nikel D (2025) Travel Chaos After Landslide Splits Norway In Two. Forbes URL https://www.forbes.com/sites/davidnikel/2025/08/30/travel-chaos-after-landslide-splits-norway-in-two/

Odenstad S (1958) Jordskredet i Göta den 7 juni 1957 : The landslide in Göta on June 7, 1957. Geologiska Föreningens i Stockholm Förhandlingar (GFF) 80(1):76–86. https://doi.org/10.1080/11035895809447207

Penna IM, Solberg IL (2021) Landscape changes and bedrock reconstruction in Gjerdrum area. Methodological approach and main results. NGU report 2021.023:82. URL https://www.ngu.no/upload/Publikasjoner/Rapporter/2021/2021 023.pdf

Quinn P, Beven K, Chevallier P, et al (1991) The prediction of hillslope flow paths for distributed hydrological modelling using digital terrain models. Hydrological Processes 5(1):59–79. https://doi.org/10.1002/hyp.3360050106

Quinn P, Diederichs M, Rowe R, et al (2012) Development of progressive failure in sensitive clay slopes. Canadian Geotechnical Journal 49(7):782–795. https://doi.org/10.1139/t2012-034

Robson BA, Hölbling D, Nielsen PR, et al (2022) Estimating the volume of the 1978 Rissa quick clay landslide in Central Norway using historical aerial imagery. Open Geosciences 14(1):252–263. https://doi.org/10.1515/ geo-2020-0331, URL https://www.degruyter.com/document/doi/10.1515/geo-2020-0331/html

Ryan I, Bruvoll A, Foldal K, et al (2021) Årsakene til kvikkleireskredet i Gjerdrum 2020 : The causes of the quick-clay landslide in Gjerdrum 2020. Gjerdrum commission report 29, Olje- og energidepartementet

SGU (2024) Quaternary deposits/Jordartsdata 1:25 000. Geological Survey of Sweden, SGU. (open data)

SHK (2009) Jordskred vid vägbygge E6 i Småröd, O län, den 20 december 2006 : Landslide during road construction E6 in Småröd, O County, December 20, 2006. Tech. Rep. RO 2009:01, Swedish Accident Investigation Board

SHK (2025) Jordskred i Stenungsund: Statens haverikommission har utrett ett jordskred i Stenungsund den 23 september 2023 : Landslide in Stenungsund. Slutrapport 2025:10, Statens haverikommission (SHK) : Swedish Accident Investigation Board

Stevens R (1983) A new sand-silt-clay triangle for textural nomenclature. Geologiska Föreningen i Stockholm Förhandlingar (GFF) 105(3):245–250. https://doi.org/10.1080/11035898309452593

Stroeven AP, Hättestrand C, Kleman J, et al (2016) Deglaciation of Fennoscandia. Quaternary Science Reviews 147:91–121. https://doi.org/https://doi.org/10.1016/j.quascirev.2015.09.016, iSBN: 7144165186

Torrance JK (2012) Landslides in quick clay. In: Landslides: types, mechanisms and modeling. Cambridge University Press, Cambridge, p 83–94

Åberg A, Andersson M, Carlsson J, et al (2023) Samhällsekonomiska effekter av jordskredet vid E6 Stenungsund : Socioeconomic effects of the landslide at E6 Stenungsund. WSP report 10361637, Föreningen Svenskt Näringsliv

Åhäll KI (1990) An investigation of the Proterozoic Stenungssund granitoid, SW Sweden; conflicting geochronological and field evidence. Mid-Proterozoic Laurentia-Baltica Geological Association of Canada Special Paper 38:117–129

Åhäll KI, Connelly JN (2008) Long-term convergence along SW Fennoscandia: 330 m.y. of Proterozoic crustal growth [Precam Res 161 (2008) 452–472]. Precambrian Research 163(3):402–421. https://doi.org/10.1016/j.precamres.2008. 02.002

Online Resource 1

Table Summarizing table over data sets used in this study. *The Swedish mapping, cadastral and land registration authority.

Dataset Type	Method/Sensor	Source	Resolution	Date	Purpose
Digital Terrain Model (DTM)	Airborne LiDAR	The Swedish mapping, cadastral and land registration authority	1m spatial c. 0.15 m vertical	6/3/2011	Interpretation of ground surface, oldest detailed elevation model
Digital Terrain Model (DTM)	Airborne LiDAR	The Swedish mapping, cadastral and land registration authority	0.3 m spatial 0.1 m vertical	3/4/2021	Interpretation of ground surface, latest detailed elevation model
Digital Terrain Model (DTM)	unknown DJI Zenmuse L1 DJI Zenmuse L2	SweScan AB Sweco Sverige AB The County Board	0.05 m 0.02 m 0.04 m	11/7/2023 09/30/2023, 10/10/2023 10/26/2023	Analyze difference of DTMs Interpret kinematics
Orthophotograph	unknown DJI Zenmuse L1 DJI Zenmuse P1 DJI Hasselblad L1D-20c DJI M3E_12.3_5280x3956	SweScan AB Sweco Sverige AB The County Board SGU Peab	0.02 m 0.02 m 0.008 m 0.08 m 0.03 m, 0.02 m	11/7/2023 09/30/2023, 10/10/2023 10/05/2023 09/27/2023 09/24/2023, 09/26/2023	Interpret kinematics
Digital Surface Model (DSM)	Derived from airborne photograph	The Swedish mapping, cadastral and land registration authority	0.3 m spatial un-spec. vertical	2016, 2018 2020, 2022	Complement for ground surface development
Orthophotograph	Airborne photograph	The Swedish mapping, cadastral and land registration authority	1 m	1995 2001	Interpret kinematics
Orthophotograph	Airborne photograph	The Swedish mapping, cadastral and land registration authority	0.5 m	1956, 1971, 2005, 2009, 2012	Interpret kinematics
Orthophotograph	Airborne photograph	The Swedish mapping, cadastral and land registration authority	0.25 m	2007, 2011, 2014 2016, 2018	Interpret kinematics
Orthophotograph	Airborne photograph	The Swedish mapping, cadastral and land registration authority	0.16 m	2020 2022	Interpret kinematics
Aerial photograph	Airborne photograph	The Swedish mapping, cadastral and land registration authority	Flight ht. 600 m Flight ht. 1200 m Flight ht. 900 m Flight ht. 900 m	1983 1988 1989 1990	Interpret and follow the construction of E6
Satellite images	Satellite	Sentinel-2		08/12/2022, 11/6/2023	Interpret and follow the ongoing construction work
InSAR	Satellite	Sentinel-1		2014-2024	Analyze ground setlements
Seismic signal	68 permanent seismic stations	The Swedish National Seismic Network (SNSN)	depends on number of station detections and distance	2023	Timing of the landslide, timing of blastings

Online Resource 2

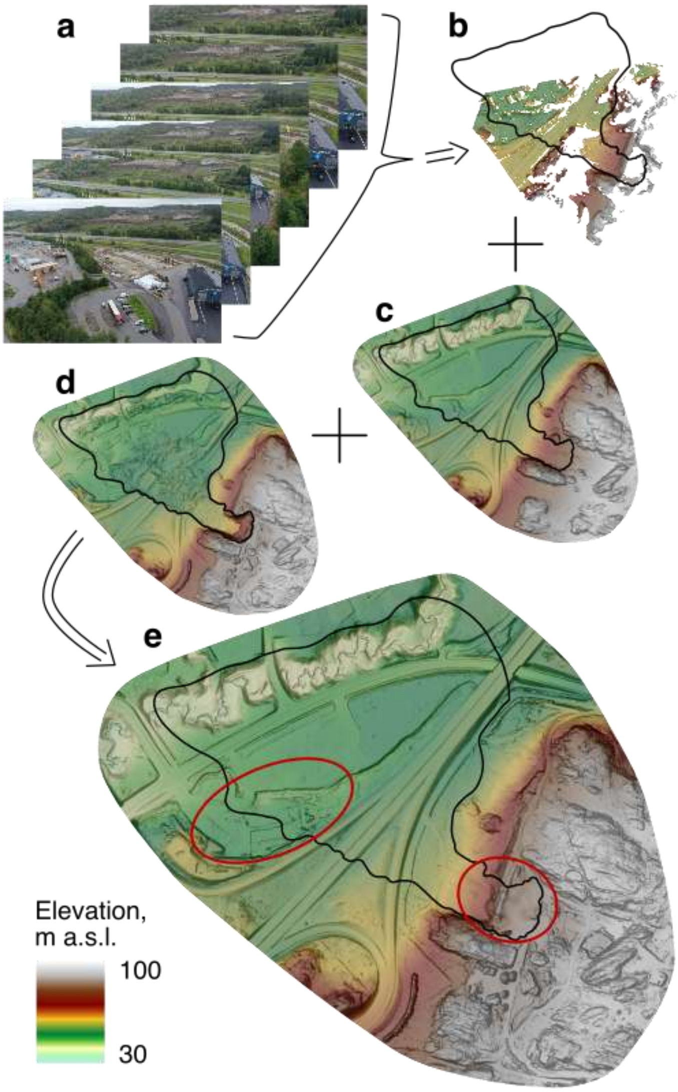

Fig. OR2 a From six photographs taken by Mikael Berglund on 20 September 2023, it was possible to recreate an orthophoto and **b** DTM of the area 2 days before the landslide. This was done by merging the significant parts of that DTM with **d** the LiDAR from after the landslide, along with the **c** latest LiDAR from before (2021). **e** Red circles mark the two areas with ongoing construction, which were critical for the reconstruction of the area. The drone multi-photo DTM had high spatial resolution but needed to be adjusted by 2-4 meters in height to align with the post-slide DTM.

Online Resource 3

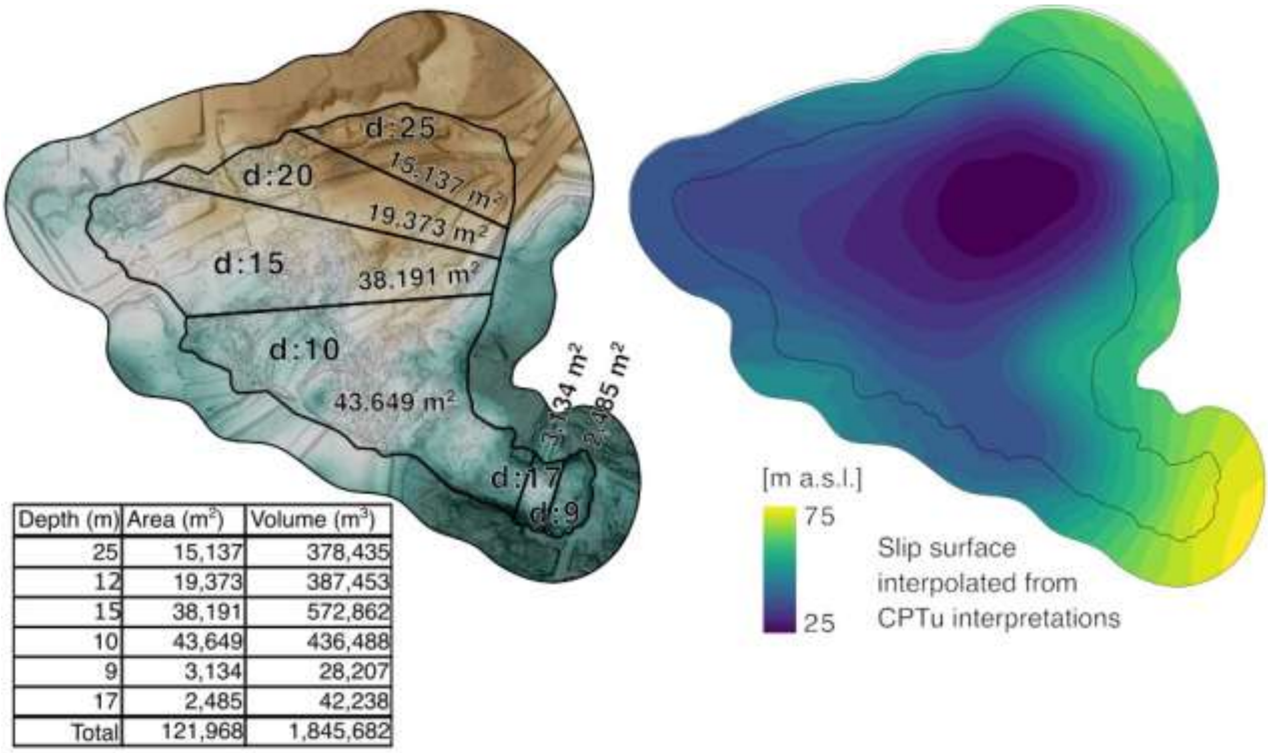

Depth (m)	Area (m²)	Volume (m³)
25	15,137	378,435
12	19,373	387,453
15	38,191	572,862
10	43,649	436,488
9	3,134	28,207
17	2,485	42,238
Total	121,968	1,845,682

Fig. OR3 The total displaced mass is estimated at 1.2–1.85 million cubic meters. The landslide area is divided into six sub-areas, each with different depth estimates from CPTu diagrams. When the volume between DTM 20230920 and the modeled 'slip surface', also in Online Resource 2, is calculated, the result is just over 1.2 million cubic meters. We interpret this to mean the total volume should be within the range of 1.2–1.85 million cubic meters. There is uncertainty in the depth estimates from CPTu interpretations used for modeling the slip surface. This model also exhibits significant edge effects, resulting in an underestimation of the volume. Other sources of uncertainty are the various resolutions in the pre-event DEM:s and re-laid material, obscuring the original surface. Another parameter to consider is the depth of the pilings in the northern area and its implications for the interpreted movements. Background: Colored bedrock model; hillshade, DTM 06/11/2023.

Online Resource 4

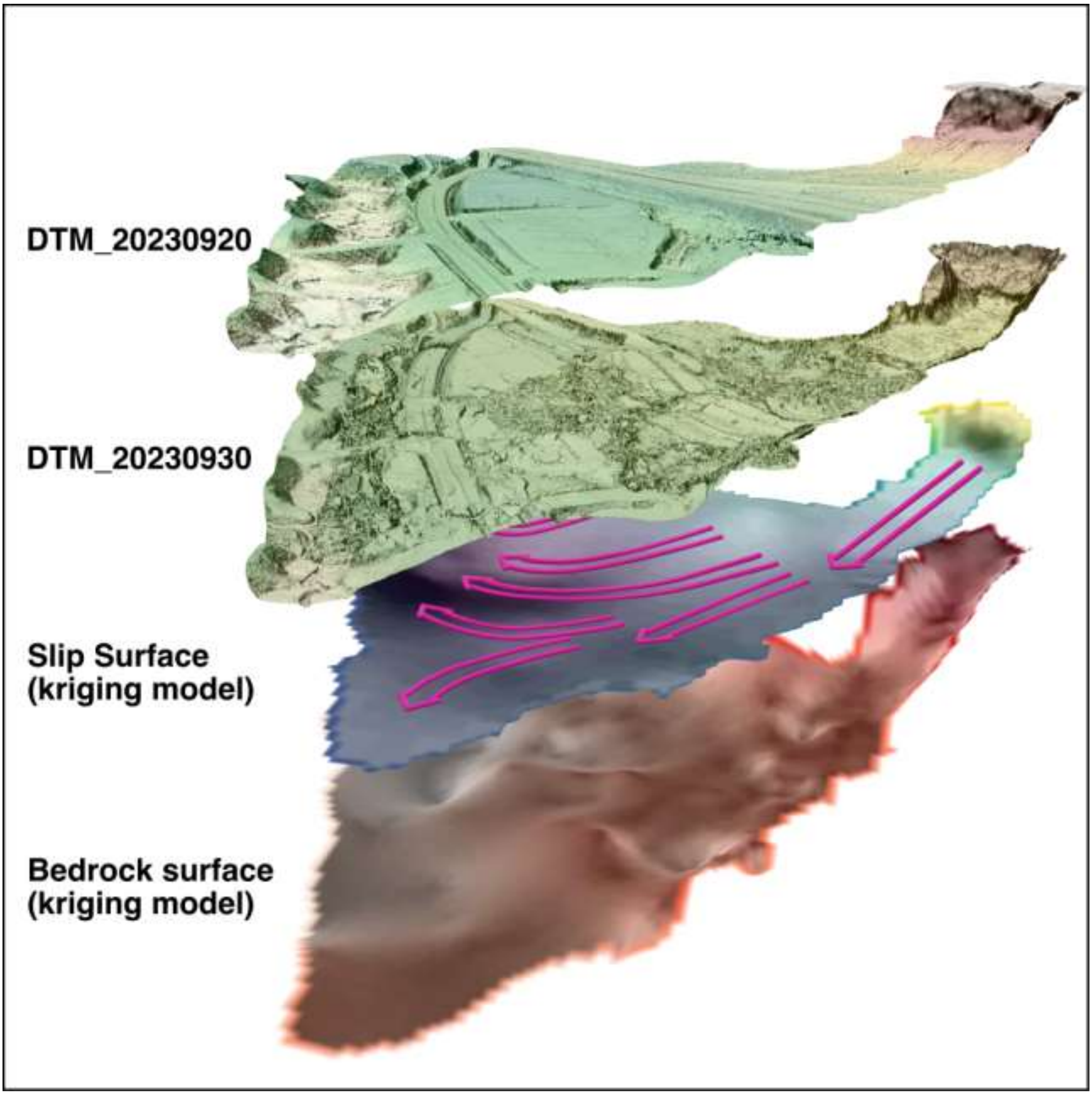

Fig. OR4 3D perspective of the surfaces in the landslide area, vertically exaggerated by 2. The ground surfaces are based on LiDAR scans from before and after the event. The two lower surfaces are modeled based on interpretations of geotechnical borehole data and field observations. CPTu diagrams are the main input for the slip surface. However, these come with significant uncertainties. In addition, the slip-surface model has significant edge effects.

Graphical Abstract